

Photogalvanic shift currents in $\text{BiFeO}_3\text{-LaFeO}_3$ superlattices

Francesco Delodovici^{*,†} and Charles Paillard^{*,‡}

[†]*Université Paris-Saclay, CentraleSupélec, CNRS, Laboratoire SPMS, 91190, Gif-sur-Yvette, France*

[‡]*Smart Ferroic Materials center, Institute of Nanosciences & Engineering and Department of Physics, University of Arkansas, Fayetteville, Arkansas 72701, USA*

E-mail: francesco.delodovici@centralesupelec.fr; paillard@uark.edu

Abstract

Designing materials with controlled photovoltaic response may lead to improved solar cells or photosensors. In this regard, ferroelectric superlattices have emerged as a rich platform to engineer functional properties. In addition, ferroelectrics are naturally endowed with a bulk photovoltaic response stemming from non-thermalized photo-excited carriers, which can overcome the fundamental limits of current solar cells. Yet, their photovoltaic output has been limited by poor optical absorption and poor charge collection or photo-excited carrier mean free path. We use Density Functional Theory and Wannierization to compute the so-called Bulk Photovoltaic shift current and the optical properties of $\text{BiFeO}_3/\text{LaFeO}_3$ superlattices. We show that, by stacking these two materials, not only the optical absorption is improved at larger wavelengths (due to LaFeO_3 smaller bandgap), but the photogalvanic shift current is also enhanced compared to that of pure BiFeO_3 , by suppressing the destructive interferences occurring between different wavelengths.

Keywords

Photogalvanic effect, shift-current, materials design, superlattices, BiFeO₃.

1 Introduction

The bulk photovoltaic (or more accurately, photogalvanic) effect (BPVE)¹ has harbored the promise of breaking the fundamental thermodynamic limit which impedes the yield of current junction-based solar cells, known as the Shockley-Queisser limit.² One of the first requirement for the BPVE is the absence of inversion symmetry. Therefore, ferroelectrics, which show a spontaneous electrical polarization that can be switched by electric fields, have been deemed particularly promising photovoltaic materials as they naturally break inversion symmetry. In fact, Spanier *et al.* showed that the Shockley-Queisser barrier could be overcome in a thin film of barium titanate,³ a prototypical ferroelectric materials. However, it has proven difficult to reach power conversion efficiencies beyond a few percents with ferroelectric-only based solar cells. This is due, in part, to the large bandgap of most ferroelectrics which start absorbing in the ultraviolet part of the solar spectrum, as well as the usually low carrier mobility exhibited by conventional ferroelectrics.^{4,5}

To circumvent these problems, many have attempted to partially modify the chemical structure of the active absorbing element. For instance, by making a solid solution involving ferroelectric KNbO₃ and oxygen deficient BaNi_{1/2}Nb_{1/2}O_{3- δ} , the bandgap of KNbO₃ is strongly reduced down to 1.4

eV.⁶ Alternatively, co-doping methods, used to improve optical absorption while limiting leakage and maintaining ferroelectric properties, have been explored but often result in localized intragap states with very limited dispersion.⁷ Perhaps most promisingly, Nechache *et al.* reached a 8.1% power conversion efficiency by stacking 3 layers of Bi(Fe,Cr)O₃ thin films with varying Cr content to enhance light absorption.⁸ This latter study, combined with the improved photovoltaic efficiency of barium titanate thin films⁹ and demonstrated enhanced collection of photo-induced charges by Atomic Force Microscopy tips,^{3,10} strongly indicate that superlattice architectures, which are periodical repeated stackings of nanolayers, may help (1) enhancing optical absorption by combining materials with different bandgaps and (2) increase the collection of photocurrents created by the bulk photovoltaic effect.

In this work, we investigate the BPVE in superlattices (SLs) of BiFeO₃ (BFO) and LaFeO₃ (LFO) by means of Density Functional Theory (DFT) calculations. The choice of these two perovskites is dictated by several natural reasons. Firstly, BFO is one of the few ferroelectrics which absorb visible light with its typical bandgap of 2.7 eV, showing for instance good piezophotocatalytic¹¹ or photovoltaic responses,^{12,13} as well as a predicted high shift current response compared to other classical ferroelectrics.¹⁴ Secondly, LFO has a smaller bandgap of about 2.34 eV,¹⁵ has been grown in superlattices with BFO^{16–18} exhibiting ferroelectric features, in particular at short periods.¹⁹ We thus expect that BFO/LFO SLs should exhibit some degree

of improved visible absorption and BPVE thanks to the complementarity of the BFO and LFO nanoscale layers.

2 Systems and methods

The linear BPVE contains two main contributions:¹ a ballistic current, caused by asymmetry in the distribution of photo-induced carriers in momentum space, and a shift current²⁰ caused by asymmetry in the spatial location of photo-induced carriers after photo-excitation. Young *et al.*^{14,21} have developed methods to calculate the latter from DFT. A third order tensor, σ_{ijk} , describes the relationship between the shift photogalvanic current density in direction i , j_i , the intensity I and polarization vector \mathbf{e} of a linearly polarized electromagnetic wave of pulsation ω ,

$$j_i = \sigma_{ijk} I e_j e_k \quad (1)$$

To calculate this tensor in BFO/LFO SLs, we performed DFT spin-polarized calculations as implemented in Quantum Espresso²² in the projected augmented wave (PAW) scheme²³ at the PBEsol²⁴ level of approximation. We included the rotationally invariant U correction, in the simplified Dudarev approach, with $U = 4.5$ eV¹⁶ to represent the on-site Coulomb interaction on Fe-ions belonging to the BFO layer, and $U = 3.65$ eV on the Fe-ions belonging to the LFO layer. This choice allows to maintain a similar bandgap

difference between bulk BFO (which we calculate at 2.26 eV here) and bulk LFO (1.83 eV calculated bandgap). We relaxed pure BFO and LFO until the maximum force was smaller than 10^{-3} eV/Å, sampling the Brillouin zone with a Monkhorst-Pack mesh with a density of at least $110 \text{ kpoints} \times \text{Å}^3$. With this choice of U, the relaxed ground state for BFO and LFO are described respectively by a pseudo-cubic lattice parameter $a = 3.977 \text{ Å}$ and an angle of $\alpha = 89.65$ degree and by an orthorhombic Pbnm phase whose primitive vectors are $a = 5.531 \text{ Å}$, $b = 5.591 \text{ Å}$, $c = 7.838 \text{ Å}$, in good agreement with the literature.¹⁶

We then considered the superlattices as if they were epitaxially grown on (001)-SrTiO₃, which is a common substrate for growing BFO films and BFO/REFO superstructures.²⁵⁻²⁷ We create the SL by alternating layers of BFO and LFO along the c direction of LFO. In this orientation, the in-plane pseudo-cubic vectors of BFO form a 45 degree angle with the in-plane primitive vectors of the superlattice, and the polarization is now directed along the [101] direction, as reported in Figure 1. The superlattice primitive vectors in Figure 1 are chosen as the lab reference frame, and all subsequent tensor components (optical dielectric permittivity, shift current tensor) refer to these axes. The mechanical effect of the substrate was simulated by fixing the in-plane lattice constant of the multi-layer to the one of cubic SrTiO₃ (previously relaxed with DFT, lattice parameter of 3.891 Å in its cubic unit cell), allowing all the remaining degrees of freedom to relax. In this con-

figuration the BFO in-plane pseudo-cubic lattice parameters are strained by -2% when comparing to the BFO relaxed bulk structure, while the \mathbf{a} and \mathbf{b} lattice parameters of LFO are strained by -0.6% and -1.6% respectively. It is known that STO substrates inhibit the cycloidal order in BFO films²⁸ leading rather to G-type antiferromagnetic (AFM) order. We thus performed spin-polarized simulations without spin-orbit coupling (SOC) to correctly describe the antiferromagnetic G-type magnetic ordering of the two pure perovskites. Past theoretical studies have shown that good agreement of the shift current with experiment could be obtained without SOC.²⁹ After relaxation, the self-consistent charge densities were employed as input to obtain Kohn-Sham wave functions from non-self consistent calculation on denser k-point meshes (of the order of 10^3 kpoints $\times\text{\AA}^3$). The resulting Kohn-Sham wave functions were then processed through Wannier90³⁰ to obtain the corresponding set of maximally-localized Wannier orbitals. A mixture of chemically sound atomic orbitals (O p , Fe p and d , Bi p , La p) were employed as an initial guess to derive the Wannier orbitals. An example of the band-structure reconstructed from Wannier orbitals is shown in Figure 2. We then obtained the electrons transport properties by post-processing the Wannier orbitals using the method described in Ref.³¹ and extracted the shift-current contribution to the BPVE in these SLs, as well as the Wannier-orbital based Kubo-formulation to obtain optical conductivity and dielectric response. We focus, in the following, on BFO₁/LFO₁ SLs structures.

3 Results

3.1 Superlattice structure

Let us first describe the relaxed structure of the different components of the $\text{BFO}_1/\text{LFO}_1$ SLs, compared to pure BiFeO_3 and LaFeO_3 . As can be observed in Figure 1, BFO bi-axially strained at the STO lattice constant exhibits its well-known R-phase structure,²⁸ characterized by a total polarization lying along the diagonal of the perovskite cube (which corresponds, in our chosen reference frame, to the $[101/2]$ direction) estimated to be $81.9 \mu\text{C}/\text{cm}^2$ and an oxygen octahedra tilt pattern $a^-a^-a^-$ in Glazer notation.³² On the other hand, strained LFO (see right panel in Figure 1) retains its $Pnma$ structure, characterized by antipolar displacements along $[100]$ direction and a tilt pattern of the form $a^-a^-c^+$. When relaxing the $\text{BFO}_1/\text{LFO}_1$ superlattice, the most stable phase shows $a^-a^-c^+$ tilt patterns, in agreement with previous reports,^{19,33} with no out-of-plane polarization but in-plane polarization along the $[100]$ axis due to the difference in the amplitude of cationic motion of La and Bi ions (see Figure 1). The space group of the relaxed superlattice is Pc .

3.2 Electronic bandstructure and optical properties

Next, we focus on the electronic bandstructure and ensuing optical properties, calculated in the Independent Particle Approximation (see Methods and Systems section). In Figure 2a, we plot the bandstructure of $\text{BFO}_1/\text{LFO}_1$.

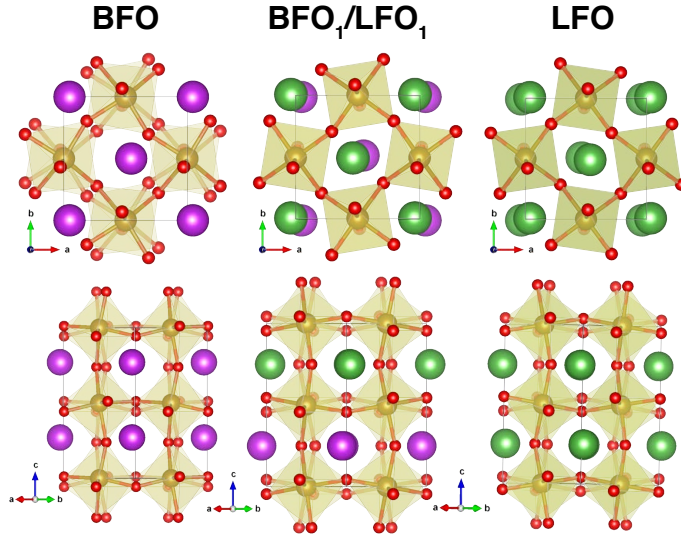


Figure 1: Calculated cells for strained BFO (left), BFO₁/LFO₁ (middle) and LFO (right); oxygen atoms are depicted in red, iron atoms in gold, bismuth in purple, and lanthanum atoms are depicted in green.

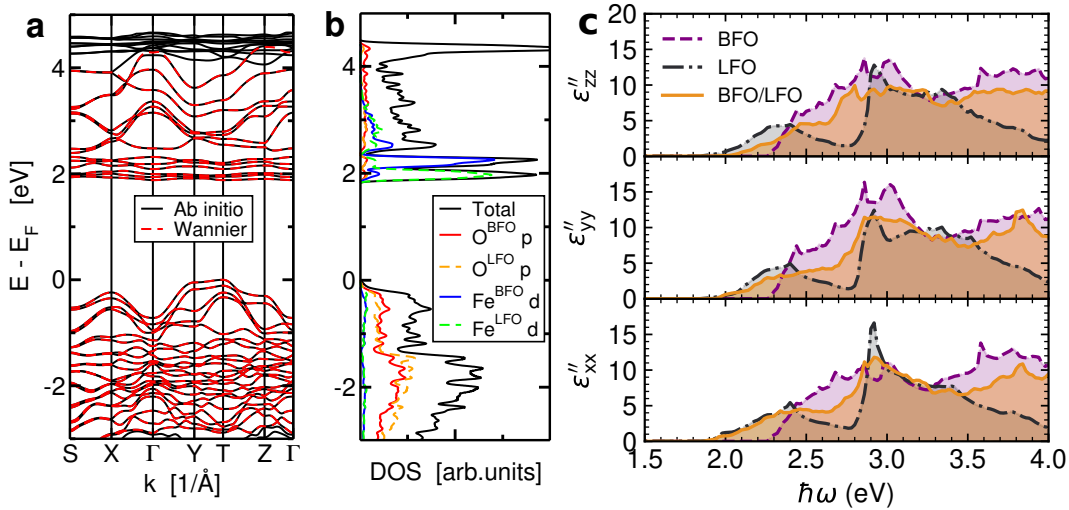


Figure 2: (a) Band structure of BFO₁/LFO₁ SL calculated from DFT (black solid lines) and from Wannier interpolation (red dashed lines). (b) Layer-by-layer decomposed Density of States in BFO₁/LFO₁ SL: dashed lines corresponds to orbitals in the LFO layer, continuous lines to those in BFO layer. (c) imaginary part of the longitudinal dielectric relative permittivity shows that the onset of BFO/LFO (yellow plain line) absorption occurs, as in LFO (black dashed-dotted lines), at lower photon energy compared to bulk BFO (purple dashed lines).

It shows that the electronic bandgap of 1.88 eV is indirect between the T and Γ point, although an almost equally large direct bandgap is present at the T point. Inspection of the atomic-decomposed Density of States (DOS) indicates that the bottom of the conduction band at Γ mainly consists of Fe d states belonging to the FeO_2 plane closer to the LaO plane (i.e. to the LFO layer). In contrast, the top of the valence band, located at the T point in the Brillouin zone, is primarily made of O $2p$ states belonging to the FeO_2 planes. Pure compressed BFO and LFO have indirect band gap too, as reported in Supplementary Information and consistent with the literature.^{15,34} The conduction (valence) bands minimum (maximum) sit at Γ (along the S-X line) in BFO, and at Γ (X) in LFO. The orbital character is preserved when the SL is formed.

Figure 2c compares the optical dielectric permittivity of $\text{BFO}_1/\text{LFO}_1$ SL, strained LFO and BFO bulk. Strained LFO, as expected, starts significantly absorbing at lower photon energies (near about 1.9 eV) compared to bulk BFO (which starts absorbing near 2.25 eV). Interestingly, the optical absorption of $\text{BFO}_1/\text{LFO}_1$ SL is dominated by the LFO layer at low photon energies (from 1.9 eV to 2.25 eV). Therefore, the SL architecture successfully manages to improve optical absorption at lower photon energies compared to pure BFO. In contrast, at larger photon energies (> 2.3 eV), the imaginary part of the relative dielectric permittivity is significantly degraded compared to pure BFO, indicating that optical absorption will be poorer than BFO at

large photon energies. Yet, the presence of BFO improves optical absorption over LFO in BFO/LFO SLs.

3.3 Shift current photogalvanic tensor

We now focus on the BPVE response of our BFO/LFO SLs. In Figure 3, we plot the shift current tensor σ_{ijk} (which relates the photogalvanic current density to the incident light intensity and polarization, see Eq. 1) for BFO₁/LFO₁ SL and bulk BFO (LFO is centrosymmetric, and thus does not exhibit a BPVE response). Interestingly, as already observed in the dielectric permittivity in Figure 2c, the shift current photo-response in BFO₁/LFO₁ SL starts at lower photon energies. For instance, in Figure 3a, the σ_{yyy} component of the shift current tensor has a finite value (near 2-6 $\mu\text{A}/\text{V}^2$), which is 20 times as large as the response of BFO for photon energies in the range 2.1-2.3 eV, *i.e.* right before the absorption edge of pure BFO.

In contrast, for photon energy larger than the calculated bandgap of BFO (≈ 2.26 eV), the magnitude of the BPVE shift current tensor in BFO₁/LFO₁ is on par or slightly smaller than BFO. To further probe the photovoltaic response of BFO₁/LFO₁, we depict polar plots in Figure 3b representing the absolute value of the photogalvanic shift current density response at selected photon energies. We assume that the visible light is polarized in the (xy) plane, *i.e.* that the polarization vector of the light is of the form $\mathbf{e} = (\cos \phi, \sin \phi, 0)$, which essentially corresponds to the case of a through-

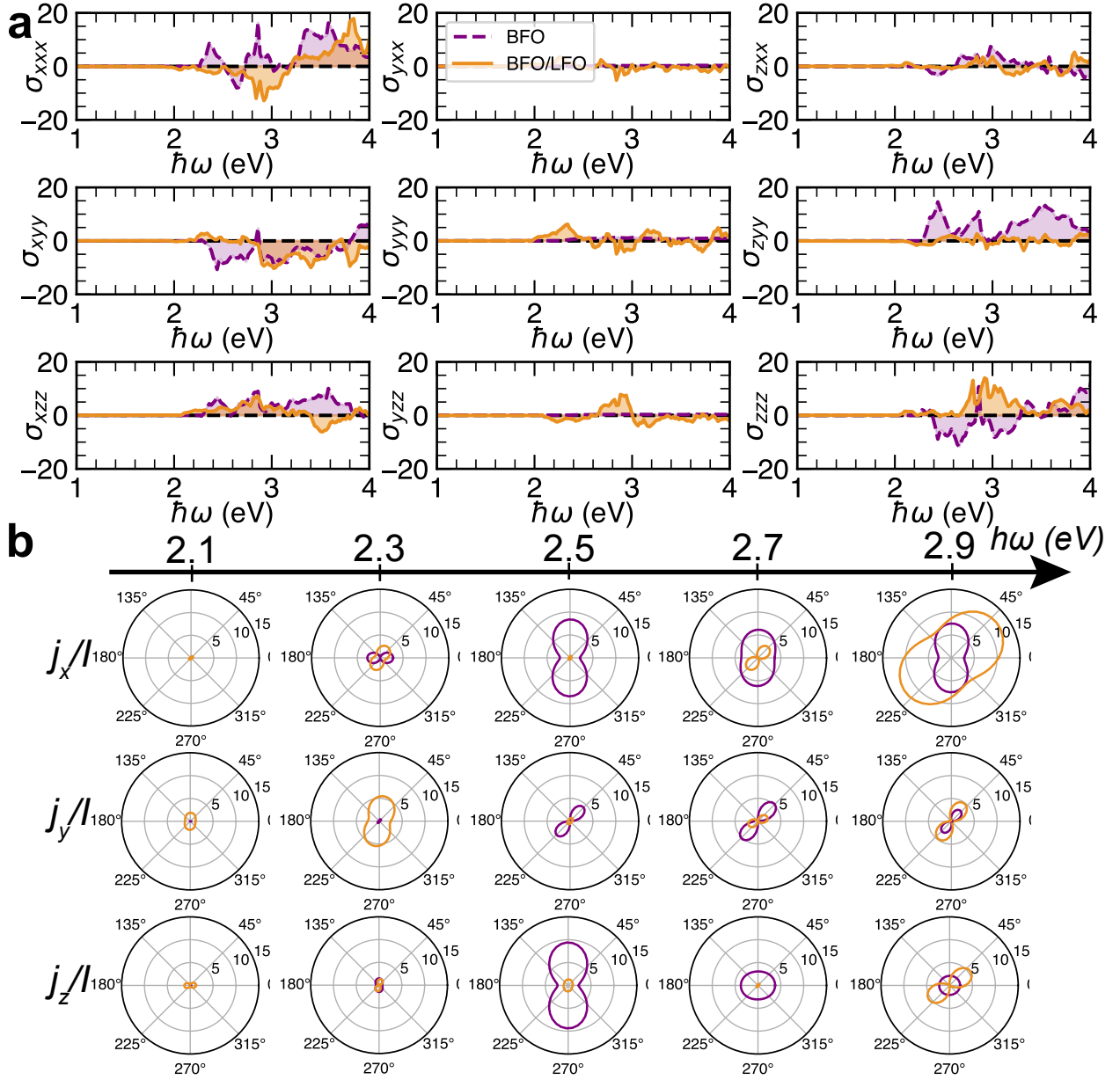


Figure 3: (a) Shift current tensor components (in $\mu\text{A} \cdot \text{V}^{-2}$) of BFO₁/LFO₁ (yellow) and bulk BFO (purple) corresponding to light linearly polarized along the lab reference frame axes. (b) polar plot showing the magnitude of the current density response j_i to light polarized in the (xy) lab reference frame for BFO₁/LFO₁ (yellow) and bulk BFO (purple).

thickness device. The results in Figure 3b clearly show that up to 2.3 eV, the shift current response of the SL is superior to that of pure BFO. This is no longer the case for photon energies of 2.5 or 2.7 eV. At further photon energies, such as 2.9 eV, a strong peak in the shift current components σ_{xxx} , σ_{xyy} and σ_{zzz} of the SL yields a large photocurrent response compared to BFO, where destructive interferences strongly reduce the photovoltaic tensor component magnitude. Note that the shift current response is shifted by about 0.7 eV when realizing calculations with the HSE hybrid functional³⁵ (see Supplementary Information).

Interestingly, various components of the BPVE shift current tensor no longer alternate sign for photon energies in the range 2-3 eV (see for instance σ_{xxx} or σ_{zzz} in Figure 3a). This is particularly interesting since, in the case of BFO, several components such as σ_{xxx} change sign with different photon energies, resulting in destructive interferences which limit the BPVE output. To further quantify the potential advantage of BFO/LFO SLs, we compute the weighted average of each components of the BPVE, with the Planck distribution as a weighted average. Specifically, we compute

$$\bar{\sigma}_{ijk}(\hbar\omega) = \frac{2}{c\varepsilon_0} \int_0^{\hbar\omega} dEB(E, T)\sigma_{ijk}(E), \quad (2)$$

where ε_0 is the vacuum permittivity, c the speed of light, $B(E, T) = \frac{2}{h^3c^2} \frac{E^3}{e^{\frac{E}{k_B T}} - 1}$ is the black body spectral radiance in $\text{W}\cdot\text{m}^{-2}\cdot\text{sr}^{-1}\cdot\text{J}^{-1}$, h the Planck constant, k_B the Boltzmann constant and $T \approx 5,777$ K the temperature of

the sun, approximated as a black body. Essentially, $\bar{\sigma}_{ijk}$ acts as a sort of Figure of Merit which integrates the shift current tensor to appropriately sum positive or destructive interferences in the photogalvanic response at different photon energies. Note that technically, we apply a small scissor shift correction to $\sigma_{ijk}(E)$ when computing $\bar{\sigma}_{ijk}(\hbar\omega)$, as we know that the calculated bandgaps of BFO and LFO are underestimated by approximately 0.5 eV compared to experimental values. The quantity $\bar{\sigma}_{ijk}(\hbar\omega)$, in the limit $\hbar\omega \rightarrow \infty$, approximates the integrated output photogalvanic current density (see Supplementary Information), and thus integrates the destructive/constructive interferences occurring due to the summation over multiple wavelengths. To further simplify the matter, we depict, in Figure 4, the quantities $\bar{j}_i(\hbar\omega) = \frac{1}{2}(\bar{\sigma}_{ixx}(\hbar\omega) + \bar{\sigma}_{iyy}(\hbar\omega))$, which approximate the photogalvanic current density under an unpolarized light traveling in the (001) direction of the SL. Figure 4 shows an important feature: the photogalvanic outputs \bar{j}_x and \bar{j}_y (i.e. for in-plane current densities generated by unpolarized light) are almost twice as large as those in pure BFO. This is due, in part, to the fact that the shift current tensor components σ_{xxx} and σ_{yyy} BFO₁/LFO₁ do not change sign over a significant range of photon energy where the Planck distribution. One may wonder whether this is related to the smaller in-plane polarization in BFO₁/LFO₁ (about 10 $\mu\text{C}/\text{cm}^2$, calculated by the Berry phase method³⁶) compared to bulk BFO (whose polarization has been measured to exceed 100 $\mu\text{C}/\text{cm}^2$ ³⁷). Although there is no straightforward relationship

between the electrical polarization and the shift current tensor,^{38,39} previous theoretical works have shown how some superlattice-like structures reduce the polar ionic cations and may lead to a strong enhancement of the integrated BPV shift current output.⁴⁰ Thus, the smaller polarization and anisotropic distortion of our BFO₁/LFO₁ SL likely favor constructive interferences compared to BFO. In contrast, the current generated in the out-of-plane direction of the SL is much smaller than in pure BFO. As our SL features no out-of-plane polarization component in the z direction, we essentially recover a mirror symmetry along z which would prevent the emergence of a photogalvanic current when light polarized along an in-plane direction is absorbed, as previously noted in a different nanolayered ferroelectric oxide in Ref.⁴⁰ Note also that the giant bulk photovoltaic effect found in the prototypical ferroelectric BaTiO₃ reported photocurrent density smaller than $10 \mu\text{A}\cdot\text{cm}^{-2}$.⁹ In contrast, BFO and LFO are both known to have smaller band gaps, and our calculated shift current tensor components such as σ_{xxx} in Figure 3 reach larger magnitude at lower photon energy compared to previous theoretical works³⁹ if one accounts for the difference in bandgaps. We thus anticipate that, given the shape of the black-body weighting function in Equation 2, BFO₁/LFO₁ would yield superior photovoltaic current density output compared to BaTiO₃ thin films.

Finally, one may wonder whether other BFO_n/LFO_m may yield larger photocurrent density than BFO₁/LFO₁. We argue that this is unlikely. In-

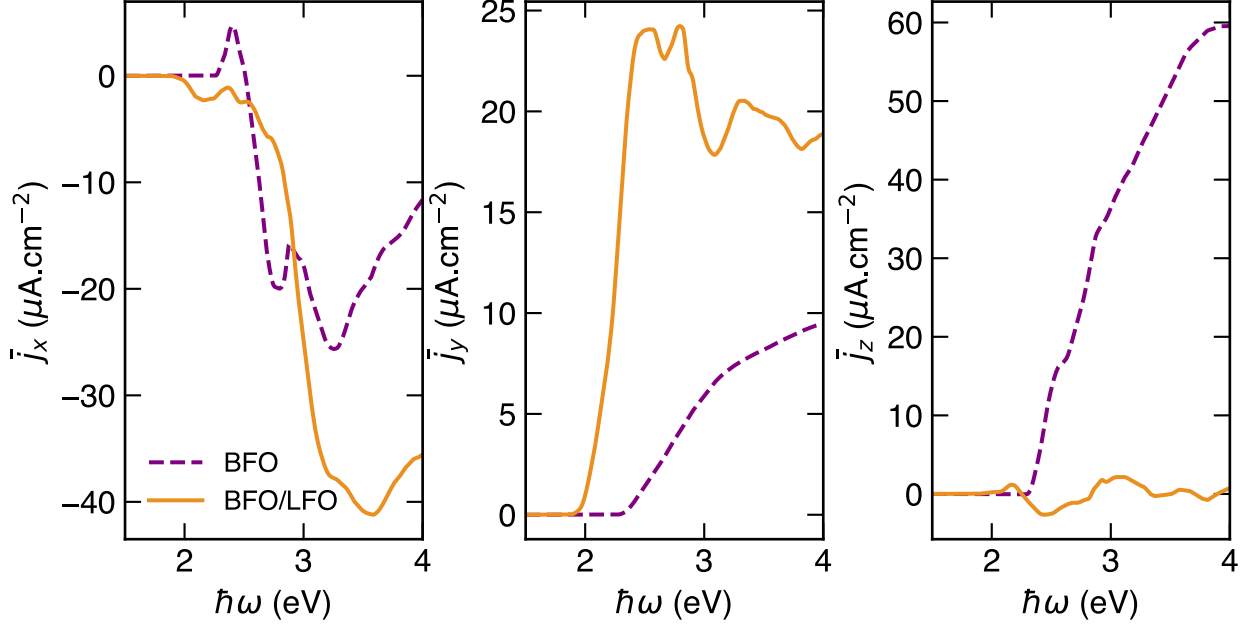


Figure 4: Integrated shift photogalvanic current using the Planck distribution as a weighting function in BFO₁/LFO₁ (yellow) and BFO (dashed purple), assuming unpolarized light.

deed, previous works indicate that for $m \geq 2$, computationally tractable BFO_n/LFO_m superlattices are centrosymmetric,¹⁶ thus preventing the shift current effect due to the presence of inversion symmetry. On the other hand, one may want to explore BFO_n/LFO₁ superlattices. Yet, it can be expected that, for large n , the photocurrent density will not be significantly improved due to the lower proportion of LFO, and thus poorer absorption at large wavelengths.

4 Conclusion

Using first-principle calculations, we show how stacking nanolayers of a ferroelectric, BiFeO₃, with a dielectric absorbing at lower photon energy (LaFeO₃)

not only increases optical absorption but may also improve the Bulk Photovoltaic shift current output. The latter improvement results from the subtle reduction in cationic displacements which, as in Ref.,³⁸ leads to the emergence of a larger range of photon energies where the shift current maintains the same direction. Our work further highlights how ferroelectric nanostructures, such as superlattices, may be used to engineer and improve the photovoltaic response of ferroelectrics. We hope that the current theoretical work will stimulate experimentalists to explore the shift current photovoltaic response of ferroelectric superlattices. The material-based, nanostructuring strategy adopted in this work is a first step toward evaluating the potential of ferroelectric superlattices for photogalvanic conversion. Future works, including the effect of bi-axial strain, temperature, as well as a system approach involving the nature of electrical contacts are needed to further optimize the photovoltaic output of multiferroic-based superlattices.

5 Supporting information

The supporting information contains: the absorption coefficient and the Glass coefficient;⁴¹ the electrons bands and the atomic-orbital projected DOS of pure perovskites; the study of the electronic band gap computed with Hybrid functional; the comparison of the full shift-conductivity tensors of pure BiFeO_3 and $\text{BFO}_1/\text{LFO}_1$ for different percentages of exact exchange and Hubbard U corrections applied.

Acknowledgement

This work was supported by Agence Nationale de la Recherche under grant agreement no. ANR-21-CE24-0032 (SUPERSPIN). This work was performed using computational resources from GENCI- TGCC (grant 2024-A0150912877) as well as from the “Mésocentre” computing center of Université Paris-Saclay, CentraleSupélec and École Normale Supérieure Paris-Saclay supported by CNRS and Région Île-de-France (<https://mesocentre.universite-paris-saclay.fr/>).

References

- (1) Sturman, B. I.; Fridkin, V. M. *The Photovoltaic and Photorefractive Effects in Noncentrosymmetric Materials*; Gordon and Breach Science Publishers, 1992.
- (2) Shockley, W.; Queisser, H. J. Detailed Balance Limit of Efficiency of p-n Junction Solar Cells. *J. Appl. Phys.* **1961**, *32*, 510.
- (3) Spanier, J. E.; Fridkin, V. M.; Rappe, A. M.; Akbashev, A. R.; Polemi, A.; Qi, Y.; Gu, Z.; Young, S. M.; Hawley, C. J.; Imbrenda, D. Power conversion efficiency exceeding the Shockley–Queisser limit in a ferroelectric insulator. *Nat. Photonics* **2016**, *10*, 611–616.
- (4) Paillard, C.; Bai, X.; Infante, I. C.; Guennou, M.; Geneste, G.;

- Alexe, M.; Kreisel, J.; Dkhil, B. Photovoltaics with Ferroelectrics: Current Status and Beyond. *Adv. Mater.* **2016**, *28*, 5153–5168.
- (5) Frye, M. B.; Garten, L. M. Reaching the Potential of Ferroelectric Photovoltaics. *Acc. Mater. Res.* **2023**, *4*, 906–909.
- (6) Grinberg, I.; West, D. V.; Torres, M.; Gou, G.; Stein, D. M.; Wu, L.; Chen, G.; Gallo, E. M.; Akbashev, A. R.; Davies, P. K.; Spanier, J. E.; Rappe, A. M. Perovskite oxides for visible-light-absorbing ferroelectric and photovoltaic materials. *Nature* **2013**, *503*, 509–512.
- (7) Hao, S.; Yao, M.; Vitali-Derrien, G.; Gemeiner, P.; Otoničar, M.; Ruello, P.; Bouyanfif, H.; Janolin, P.-E.; Dkhil, B.; Paillard, C. Optical absorption by design in a ferroelectric: co-doping in BaTiO₃. *J. Mater. Chem. C* **2022**, *10*, 227–234.
- (8) Nechache, R.; Harnagea, C.; Li, S.; Cardenas, L.; Huang, W.; Chakrabartty, J.; Rosei, F. Bandgap tuning of multiferroic oxide solar cells. *Nat. Photonics* **2015**, *9*, 61–67.
- (9) Zenkevich, A.; Matveyev, Y.; Maksimova, K.; Gaynutdinov, R.; Tolstikhina, A.; Fridkin, V. Giant bulk photovoltaic effect in thin ferroelectric BaTiO₃ films. *Phys. Rev. B* **2014**, *90*, 161409.
- (10) Alexe, M.; Hesse, D. Tip-enhanced photovoltaic effects in bismuth ferrite. *Nat. Commun.* **2011**, *2*, 256.

- (11) Amdouni, W.; Fricaudet, M.; Otoničar, M.; Garcia, V.; Fusil, S.; Kreisel, J.; Maghraoui-Meherzi, H.; Dkhil, B. BiFeO₃ Nanoparticles: The “Holy-Grail” of Piezo-Photocatalysts? *Adv. Mater.* **2023**, *35*, 2301841.
- (12) Choi, T.; Lee, S.; Choi, Y. J.; Kiryukhin, V.; Cheong, S.-W. Switchable ferroelectric diode and photovoltaic effect in BiFeO₃. *Science (New York, N.Y.)* **2009**, *324*, 63–66.
- (13) Yang, S.; Martin, L. W.; Byrnes, S. J.; Conry, T. E.; Basu, S. R.; Paran, D.; Reichertz, L.; Ihlefeld, J.; Adamo, C.; Melville, A.; Chu, Y. H.; Yang, C.-H.; Musfeldt, J. L.; Schlom, D. G.; Ager, J. W.; Ramesh, R. Photovoltaic effects in BiFeO₃. *Appl. Phys. Lett.* **2009**, *95*, 62909.
- (14) Young, S. M.; Zheng, F.; Rappe, A. M. First-Principles Calculation of the Bulk Photovoltaic Effect in Bismuth Ferrite. *Phys. Rev. Lett.* **2012**, *109*, 236601.
- (15) Scafetta, M. D.; Cordi, A. M.; Rondinelli, J. M.; May, S. J. Band structure and optical transitions in LaFeO₃: theory and experiment. *J. Condens. Matter Phys.* **2014**, *26*, 505502.
- (16) Rispens, G.; Ziegler, B.; Zanolli, Z.; Íñiguez, J.; Ghosez, P.; Paruch, P. Phase diagram of BiFeO₃/LaFeO₃ superlattices studied by x-ray diffrac-

- tion experiments and first-principles calculations. *Phys. Rev. B* **2014**, *90*, 104106.
- (17) Carcan, B.; Bouyanfif, H.; Marssi, M. E.; Marrec, F. L.; Dupont, L.; Davoisne, C.; Wolfman, J.; Arnold, D. C. Interlayer strain effects on the structural behavior of BiFeO₃ /LaFeO₃ superlattices. *J. Appl. Phys.* **2018**, *124*, 44105.
- (18) Gu, R.; Xu, R.; Delodovici, F.; Carcan, B.; Khiari, M.; Vaudel, G.; Juvé, V.; Weber, M. C.; Poirier, A.; Nandi, P.; Xu, B.; Gusev, V. E.; Bellaiche, L.; Laulhé, C.; Jaouen, N.; Manuel, P.; Dkhil, B.; Paillard, C.; Yedra, L.; Bouyanfif, H.; Ruello, P. Superorders and terahertz acoustic modes in multiferroic BiFeO₃/LaFeO₃ superlattices. *Appl. Phys. Rev.* **2024**, *11*, 041415.
- (19) Zanolli, Z.; Wojdeł, J. C.; Íñiguez, J.; Ghosez, P. Electric control of the magnetization in BiFeO₃/LaFeO₃ superlattices. *Phys. Rev. B* **2013**, *88*, 060102.
- (20) Resta, R. Geometrical Theory of the Shift Current in Presence of Disorder and Interaction. *Phys. Rev. Lett.* **2024**, *133*, 206903.
- (21) Young, S. M.; Rappe, A. M. First Principles Calculation of the Shift Current Photovoltaic Effect in Ferroelectrics. *Phys. Rev. Lett.* **2012**, *109*, 116601.

- (22) Giannozzi, P.; Baroni, S.; Bonini, N.; Calandra, M.; Car, R.; Cavazzoni, C.; Ceresoli, D.; Chiarotti, G. L.; Cococcioni, M.; Dabo, I.; Dal Corso, A.; de Gironcoli, S.; Fabris, S.; Fratesi, G.; Gebauer, R.; Gerstmann, U.; Gougoussis, C.; Kokalj, A.; Lazzeri, M.; Martin-Samos, L.; Marzari, N.; Mauri, F.; Mazzarello, R.; Paolini, S.; Pasquarello, A.; Paulatto, L.; Sbraccia, C.; Scandolo, S.; Sclauzero, G.; Seitsonen, A. P.; Smogunov, A.; Umari, P.; Wentzcovitch, R. M. QUANTUM ESPRESSO: a modular and open-source software project for quantum simulations of materials. *J. Condens. Matter Phys.* **2009**, *21*, 395502.
- (23) Blöchl, P. E. Projector augmented-wave method. *Phys. Rev. B* **1994**, *50*, 17953–17979.
- (24) Perdew, J. P.; Ruzsinszky, A.; Csonka, G. I.; Vydrov, O. A.; Scuseria, G. E.; Constantin, L. A.; Zhou, X.; Burke, K. Restoring the Density-Gradient Expansion for Exchange in Solids and Surfaces. *Phys. Rev. Lett.* **2008**, *100*, 136406.
- (25) Khaled, M. A.; Arnold, D. C.; Dkhil, B.; Jouiad, M.; Hoummada, K.; El Marssi, M.; Bouyanfif, H. Anti-polar state in BiFeO₃/NdFeO₃ superlattices. *J. Appl. Phys.* **2021**, *130*, 244101.
- (26) Maran, R.; Yasui, S.; Eliseev, E. A.; Glinchuk, M. D.; Morozovska, A. N.; Funakubo, H.; Takeuchi, I.; Nagarajan, V. Interface control of a mor-

- phototropic phase boundary in epitaxial samarium modified bismuth ferrite superlattices. *Phys. Rev. B* **2014**, *90*, 245131–245142.
- (27) Maran, R.; Yasui, S.; Eliseev, E.; Morozovska, A.; Funakubo, H.; Takeuchi, I.; Valanoor, N. Enhancement of Dielectric Properties in Epitaxial Bismuth Ferrite–Bismuth Samarium Ferrite Superlattices. *Adv. Electron. Mater.* **2016**, *2*, 1600170.
- (28) Sando, D.; Agbelele, A.; Rahmedov, D.; Liu, J.; Rovillain, P.; Toulouse, C.; Infante, I.; Pyatakov, A.; Fusil, S.; Jacquet, E.; others Crafting the magnonic and spintronic response of BiFeO₃ films by epitaxial strain. *Nat. mater.* **2013**, *12*, 641–646.
- (29) Young, S. M.; Zheng, F.; Rappe, A. M. First-Principles Calculation of the Bulk Photovoltaic Effect in Bismuth Ferrite. *Phys. Rev. Lett.* **2012**, *109*, 236601.
- (30) Pizzi, G.; Vitale, V.; Arita, R.; Blügel, S.; Freimuth, F.; Géranton, G.; Gibertini, M.; Gresch, D.; Johnson, C.; Koretsune, T.; Ibañez-Azpiroz, J.; Lee, H.; Lihm, J.-M.; Marchand, D.; Marrazzo, A.; Mokrousov, Y.; Mustafa, J. I.; Nohara, Y.; Nomura, Y.; Paulatto, L.; Poncé, S.; Ponweiser, T.; Qiao, J.; Thöle, F.; Tsirkin, S. S.; Wierzbowska, M.; Marzari, N.; Vanderbilt, D.; Souza, I.; Mostofi, A. A.; Yates, J. R. Wannier90 as a community code: new features and applications. *J. Condens. Matter Phys.* **2020**, *32*, 165902.

- (31) Ibañez Azpiroz, J.; Tsirkin, S. S.; Souza, I. Ab initio calculation of the shift photocurrent by Wannier interpolation. *Phys. Rev. B* **2018**, *97*, 245143.
- (32) Glazer, A. M. The classification of tilted octahedra in perovskites. *Acta Crystallogr. B* **1972**, *28*, 3384–3392.
- (33) Xu, R.; Delodovici, F.; Dkhil, B.; Paillard, C. Oxygen tilt driven polar superorders in BiFeO₃-based superlattices. *Phys. Rev. B* **2024**, *109*, L220101.
- (34) Paillard, C.; Xu, B.; Dkhil, B.; Geneste, G.; Bellaiche, L. Photostriction in Ferroelectrics from Density Functional Theory. *Physical Review Letters* **2016**, *116*, 247401.
- (35) Heyd, J.; Scuseria, G. E.; Ernzerhof, M. Hybrid functionals based on a screened Coulomb potential. *J. Chem. Phys.* **2003**, *118*, 8207–8215.
- (36) King-Smith, R. D.; Vanderbilt, D. Theory of polarization of crystalline solids. *Phys. Rev. B* **1993**, *47*, 1651–1654.
- (37) Lebeugle, D.; Colson, D.; Forget, A.; Viret, M. Very large spontaneous electric polarization in BiFeO₃ single crystals at room temperature and its evolution under cycling fields. *Appl. Phys. Lett.* **2007**, *91*, 022907.
- (38) Tan, L. Z.; Zheng, F.; Young, S. M.; Wang, F.; Liu, S.; Rappe, A. M.

Shift current bulk photovoltaic effect in polar materials—hybrid and oxide perovskites and beyond. *Npj Comput. Mater.* **2016**, *2*, 1–12.

- (39) Young, S. M.; Rappe, A. M. First Principles Calculation of the Shift Current Photovoltaic Effect in Ferroelectrics. *Phys. Rev. Lett.* **2012**, *109*, 116601.
- (40) Wang, F.; Young, S. M.; Zheng, F.; Grinberg, I.; Rappe, A. M. Substantial bulk photovoltaic effect enhancement via nanolayering. *Nat. Commun.* **2016**, *7*, 10419.
- (41) Ibañez-Azpiroz, J.; Souza, I.; de Juan, F. Directional shift current in mirror-symmetric BC₂N. *Phys. Rev. Res.* **2020**, *2*, 013263.